

CML

Computer Mechanics Laboratory

Technical Report No. 02-018

***THE EFFECTS OF E-BLOCK ARM THICKNESS
ON HEAD VIBRATION BETWEEN CO-ROTATING DISKS
IN A MODELED HARD DISK DRIVE***

Hany M. Gross, David B. Bogy, and Ömer Savas

Computer Mechanics Laboratory

Department of Mechanical Engineering

University of California, Berkeley 94720-1740

Toru Watanabe

HDD Division, Fujitsu Ltd.

4-4-1 Kamikodanaka, Nakahara-ku,

Kawasaki, 211-8588, Japan

December 2002

Abstract

In this work, the flow-induced off-track vibration of a read/write head between co-rotating disks was investigated experimentally. In particular, the effect of E-block arm thickness on the head vibration in the off-track direction was investigated in a modeled disk drive prepared for this study. Four different E-block arm thicknesses were used, ranging from 1.0 mm to 1.6 mm in steps of 0.2 mm. Two head gimbal assemblies were attached to each E-block arm, and they were inserted between two co-rotating disks, rotating at 10,000 rpm, and fixed at a disk spacing of 2.0 mm. Head vibration in the off-track direction was measured using a laser Doppler vibrometer at the inner diameter, the middle diameter, and the outer diameter radial positions. The frequency range considered was 0-20 kHz. Finite element analysis was used to compute the natural frequencies and mode shapes of the head gimbal assemblies, the E-block arms, and the head stack assemblies, in order to identify the resonances observed in the experimental measurements.

The primary contributors to the measured head off-track vibration were identified as the E-block arm sway mode, the suspension second torsion mode, and the suspension sway mode. The off-track RMS amplitude was determined over four frequency bands in the measurement range in order to assess the contributions of the E-block arm dynamics and the suspension dynamics to the off-track RMS amplitude.

Table of Contents

<i>Section</i>	<i>page</i>
Abstract	ii
Table of Contents	iii
List of Tables	iv
List of Figures	v
1. Introduction	1
2. Experimental Setup	3
3. Finite Element Modeling and Analysis	5
4. Experimental Results and Discussion	7
5. Conclusion	13
6. Acknowledgements	14
7. References	15

List of Tables

Table 1	HGA natural frequencies and mode shapes of active modes in 0-20 kHz range.
Table 2	E-block arm natural frequencies and mode shapes of first five modes.
Table 3	FEA results for the natural frequencies and mode shapes of the HSA modes that were identified in the experimental measurements.
Table 4	Estimates of the frequencies of the three dominant resonant peaks observed in the measured spectra.
Table 5	RMS amplitudes [nm] of the slider off-track vibration over the 0-20 kHz frequency range.
Table 6	RMS component amplitudes [nm] of the slider off-track vibration over the 0-2 kHz frequency range.
Table 7	RMS component amplitudes [nm] of the slider off-track vibration over the 2-20 kHz frequency range.
Table 8	Reynolds number at OD for different arm thicknesses.
Table 9	RMS component amplitudes [nm] of the slider off-track vibration over the 2-6 kHz frequency range.
Table 10	RMS component amplitudes [nm] of the slider off-track vibration over the 6-10 kHz frequency range.
Table 11	RMS component amplitudes [nm] of the slider off-track vibration over the 10-20 kHz frequency range.

List of Figures

- Figure 1 Modeled disk drive.
- Figure 2 A close-up of the HSA.
- Figure 3 A close-up of the HGA.
- Figure 4 ANSYS model of pico-CAPS HGA.
- Figure 5 ANSYS model of E-block arm.
- Figure 6 Variation of the natural frequencies of the first five E-block modes as a function of E-block arm thickness.
- Figure 7 ANSYS HSA model.
- Figure 8 Variation of resonant frequencies of different thickness arms.
- Figure 9 Power spectrum of slider off-track vibration, 1.0 mm thickness arm.
- Figure 10 Power spectrum of slider off-track vibration, 1.2 mm thickness arm.
- Figure 11 Power spectrum of slider off-track vibration, 1.4 mm thickness arm.
- Figure 12 Power spectrum of slider off-track vibration, 1.6 mm thickness arm.
- Figure 13 RMS amplitudes [nm] of the slider off-track vibration over the 0-20 kHz frequency range.
- Figure 14 RMS component amplitudes [nm] of the slider off-track vibration over the 0-2 kHz frequency range.
- Figure 15 RMS component amplitudes [nm] of the slider off-track vibration over the 2-20 kHz frequency range.
- Figure 16 RMS component amplitudes [nm] of the slider off-track vibration over the 2-6 kHz frequency range.
- Figure 17 RMS component amplitudes [nm] of the slider off-track vibration over the 6-10 kHz frequency range.
- Figure 18 RMS component amplitudes [nm] of the slider off-track vibration over the 10-20 kHz frequency range.

1. Introduction

The hard disk drive (HDD) industry is faced with demands for higher areal recording densities, faster data transfer rates, and a higher reliability. The areal recording density can be increased by increasing the track density and the linear bit density. Track densities beyond 40,000 tracks per inch (TPI) have already been implemented in current disk drives, and higher density objectives have made their way into industry roadmaps. Track misregistration (TMR) must be reduced in order to achieve such high track densities. On the other hand, the demand for higher data transfer rates has resulted in faster disk rotation speeds, which, in turn, has led to greater flow velocities, hence increasing the aerodynamic forces in the drive. These forces excite the head gimbal assemblies (HGA's) and the E-block arms, inducing head vibration.

Early research on the effects of airflow in hard disk drives on suspension vibration was carried out by Yamaguchi *et al.* [1]. The findings in [1] indicated that the amplitude of suspension vibration was proportional to the square of the approaching velocity. In subsequent research by Yamaguchi *et al.* [2, 3], the flow around a suspension was measured using hot-wire anemometry to identify the sources of suspension vibration, and numerical simulations of the flow were carried out. It was shown in [2, 3] that suspension vibration was caused by the turbulence behind the suspension cross-section, and that applying an aerofoil shape to the suspension cross-section can reduce suspension vibration.

The flow field between co-rotating disks that are fully shrouded by a cylindrical wall was numerically investigated by Iglesias *et al.* [4]. The research in [4] concluded that there were significant vertical velocity fluctuations at the disk outer region, which resulted in disk flutter. The presence of the E-block arm between the disks in an actual disk drive gives rise to a more complicated flow structure, which prompts an investigation of the effects of the arm on the flow between disks. Abrahamson *et al.* [5] performed flow visualization experiments using a dye-injection technique on a modeled realistic disk drive, but without considering the effects of the HGA. Vortex shedding from the arm tip was observed. Harrison *et al.* [6] measured the flow field around an arm using hot-wire anemometry. It was shown in [6] that the mean flow velocity increased as the disks were shrouded and/or as the disk spacing was decreased. A numerical investigation of the flow around the arm was performed by Suzuki *et al.* [7], where it was shown that the insertion of the arm between co-rotating disks causes disk flutter and power losses due to windage.

A transverse type arm was used in the studies carried out in studies [4, 5, 6, 7]. Current disk drives, however, employ in-line type arm/suspension assemblies. Flow visualization experiments for in-line type arm/suspension assemblies were carried out by Girard *et al.* [8]. Vortex shedding around the arm tip was observed. However, the flow-induced vibration of the E-block arm and the suspension, and its associated effects on TMR, were not investigated.

In this study, the flow-induced vibration in the off-track direction of a read/write head between co-rotating disks was investigated experimentally. In particular, the effect of E-block arm thickness on the head off-track vibration was investigated in a modeled drive, prepared for this work. Four different E-block arm thicknesses were used, ranging from 1.0 mm to 1.6 mm in steps of 0.2 mm. Two HGA's were attached to each E-block arm, and they were inserted between two co-rotating disks, spinning at 10,000 rpm, and fixed at a disk spacing of 2.0 mm. Head vibration in the off-track direction was measured using a laser Doppler vibrometer (LDV) at three radial positions: the inner diameter (ID), the middle diameter (MD), and the outer diameter (OD). The frequency range considered was 0-20 kHz. Finite element analysis (FEA) was used to compute the natural frequencies and mode shapes of the HGA, the E-block arms, and the head stack assemblies (HSA), in order to identify the resonances observed in the experimental measurements.

2. Experimental Setup

The modeled drive shown in Fig. 1 was prepared for this study. The setup consists of a fixed plate A, to which the E-block is completely fixed using a screw; and a movable plate B, on which the spindle, the shroud, and the rest of the enclosure are mounted. The E-block, shown in Fig. 2, does not have a pivot and a coil, and it does not rotate to seek different radial positions on the disks. Instead, the head is moved to different radial positions by rotating plate B, and consequently the spindle and disks, about an axis that

corresponds to the actual pivot of the E-block. The precision of positioning the head at the ID, MD, and OD was achieved through the use of pins that fit in carefully located holes on plate A. This arrangement was used in order to allow for changing the radial position of the head without changing the relative position between the head and the air table on which the experimental setup was mounted. This was very convenient for measuring the head vibration using an LDV since it eliminated the need to readjust the LDV head and cable to reestablish beam alignment and focus.

The spindle used in the setup was an actual drive ball bearing spindle, and it was operated at 10,000 rpm in this study. A cross plate – Fig. 1(b) – was used to support the spindle at the top in order to reduce spindle vibrations. Fujitsu's pico-CAPS suspensions for pico-sliders (Fig. 3) were used in this experiment. The loadbeam cross-section of the pico-CAPS suspension is rectangular, and is flangeless. Four different E-block arm thicknesses were tested: 1.0 mm, 1.2 mm, 1.4 mm and 1.6 mm. Two HGA's were attached, using an adhesive, to each arm, and were inserted between two 84 mm diameter platters, fixed at a disk spacing of 2.0 mm. A POLYTEC OFV-1102 LDV was used for taking the measurements, and its output was fed to an HP3562A signal analyzer to obtain the power spectra. The slider vibration in the off-track direction was measured at the ID, MD, and OD, for each of the arm thicknesses above, giving a total of twelve measurement sets. For each arm thickness, all measurements were repeated on two identical HSA samples to ensure consistency of the results.

3. Finite Element Modeling and Analysis

3.1. Head Gimbal Assembly

The pico-CAPS HGA was modeled in ANSYS as shown in Fig. 4. The baseplate, loadbeam, and slider were modeled using SOLID45 3-D structural solid elements. MASS21 structural mass elements were used to account for the added inertias of the trace, the damping layers on the suspension, the flexible printed circuit terminal, and the gold balls used to ensure electrical connection between the slider and the trace. The position of the printed circuit terminal is not the same for the upper and lower HGA's. ANSYS modal analysis was used to compute the natural frequencies and associated mode shapes of the active modes of the upper and lower HGA's in the 0-20 kHz frequency range. The results are presented in Table 1.

3.2. E-Block Arm

The E-block arm was modeled in ANSYS as shown in Fig. 5. The arm was modeled using SOLID45 3-D structural solid elements. The natural frequencies and associated mode shapes of the E-block arm were computed using ANSYS modal analysis for each arm thickness. The results are presented in Table 2 for the first five modes. The variation of the natural frequencies of these modes as a function of E-block arm thickness is shown in Fig. 6. Note that the natural frequency of the sway mode is less sensitive to the change in arm thickness than the natural frequencies of the other modes.

3.3. Head Stack Assembly

The HSA in this study consisted of a single E-block arm and two HGA's. The HSA was modeled by combining the component models described above, as illustrated in Fig. 7. The natural frequencies and associated mode shapes of the HSA were obtained using ANSYS modal analysis for each arm thickness. The HSA active modes in the 0-20 kHz range are numerous due to the dynamic coupling between the upper and lower HGA modes, and the dynamic coupling between the HGA modes and the E-block arm modes. A complete list of these modes is not provided. Table 3 lists the FEA results for the natural frequencies and mode shapes of the HSA modes that were identified in the experimental measurements. The first mode listed in Table 3 is dominated by the E-block arm sway mode, which drives the suspension sway mode. It should be noted that the slope of variation of natural frequency of this mode as a function of E-block arm thickness is roughly the same as that of the variation of the natural frequency of the E-block arm sway mode as a function of arm thickness, as presented in §3.2. This is illustrated in Fig. 8.

4. Experimental Results and Discussion

The power spectra of the slider off-track vibration for the different arm thicknesses are shown in Figs. 9 through 12. All of these spectra exhibit three dominant resonance peaks, the frequencies for which are listed in Table 4. The first resonance peak occurred at a frequency of around 8 kHz, and was identified as the E-block arm sway mode coupled with the suspension sway mode (the first mode in Table 3). The discrepancy between the frequencies computed using FEA and those obtained experimentally can be attributed to the incompleteness and simplicity of the FE model. Nonetheless, the congruence of the slope of the variation of the frequency of the measured resonance and that of the variation of the natural frequency of the E-block arm sway/suspension sway mode presented in §3.3 is a clear indicator that the observed mode is, in fact, the identified one (Fig. 8).

The second and third major resonance peaks in the measured spectra occurred at frequencies of around 12 kHz and 14 kHz, respectively. The 12 kHz resonance peak was identified as the second torsion mode of the HGA; the 14 kHz resonance peak was identified as the sway mode of the HGA. Note that the frequencies of these two peaks are relatively insensitive to changes in the E-block arm thickness. The power spectra of the slider off-track vibration for the 1.0 mm thick E-block arm (Fig. 9) also contain two small peaks at 2.65 kHz and 5.7 kHz. The former peak is the first bending mode of the HGA, and the latter is the base plate first bending mode coupled with the HGA second bending mode. The amplitude of the 2.65 kHz peak is lower than the amplitudes of the three

major modes in the spectra by more than 10 dB, and the amplitude of the 5.7 kHz peak is lower than the amplitudes of the three major modes by more than 20 dB. Consequently, the contributions of these two modes to the slider off-track motion are relatively small.

If the root mean square (RMS) power spectrum is expressed as $P_{rms}(f)$ as a function of frequency, f , then the total RMS amplitude, A_{rms} , can be written as

$$A_{rms} = \sqrt{h \sum_i P_{rms}(f_i)} \quad (1)$$

where h is a scale factor for the windowing function. A Hanning window was used in these measurements. It should be noted that the relationship expressed in Eq. (1) is a Pythagorean relationship, and that it applies for different frequency ranges. The RMS amplitude of the slider off-track vibration was evaluated for each E-block arm thickness over the 0-20 kHz frequency range. These RMS amplitudes are listed in Table 5 and are plotted in Fig. 13. A common feature of all the off-track vibration power spectra presented in Figs. 9 through 12 is that the amplitude of the slider off-track vibration increased as the slider was moved from the ID to the MD to the OD. This is clearly evident in Fig. 13. Figure 13 also shows that the RMS amplitudes of the slider vibration increased as the E-block arm thickness was increased.

The RMS amplitudes over the 0-20 kHz range were broken down into two components: a component over the 0-2 kHz frequency range, and a component over the 2-20 kHz range. The amplitudes of these components are listed in Tables 6 and 7, and are presented in Figs. 14 and 15, respectively. It is clear that the component amplitudes over both frequency ranges increased as the slider was moved from the ID to the OD.

Furthermore, the component amplitudes over the 0-2 kHz range increased as the E-block arm thickness was increased. On the other hand, the trend that the 2-20 kHz component amplitudes followed as the E-block arm thickness was increased was somewhat unexpected. The amplitudes of these components increased as the arm thickness was increased from the 1.0 mm to 1.2 mm. They attained their highest values at the 1.2 mm thickness and then decreased as the arm thickness was increased to attain their lowest values at the 1.6 mm thickness for all radial positions.

The trend that the 0-2 kHz component amplitudes followed as the E-block arm thickness was increased may be explained by postulating that increasing the arm thickness led to higher levels of turbulence in the flow, hence resulting in greater levels of fluctuation in the aerodynamic forces in the drive. Such fluctuations may have induced higher disk flutter and higher levels of HSA vibrations, which, in turn, generated greater levels of slider vibration.

The trend observed for the 2-20 kHz components was quite interesting, and may be explained as the combination of two effects. The first effect can be explained by noting that if the same external forces are applied to each E-block arm, then the amplitude of the arm sway mode must decrease as the arm thickness is increased, due to the increase in inertia and the increase in stiffness that accompany the increase in arm thickness. This explains the decline in amplitude observed going from the 1.2 mm arm thickness to the 1.6 mm arm thickness. The increase in the RMS amplitude components as the arm thickness was increased from 1.0 mm to 1.2 mm may be explained by the

second effect, which is the increase in the flow fluctuation levels and the drag force as the arm thickness was increased. In general, the drag force D is proportional to the square of the flow velocity, and can be expressed in terms of the fluid density ρ ; the flow velocity U , the area S normal to the flow, and the drag coefficient C_D , as

$$D = \frac{1}{2} \rho U^2 S C_D \quad (2).$$

In the case at hand, the drag force can be broken down into a friction drag force, and a pressure drag force. The friction drag D_f and the pressure drag D_p can be expressed as

$$D_f = \int_A \hat{\tau} dA \quad (3),$$

$$D_p = \int_S p dS \quad (4),$$

where $\hat{\tau}$ is the shear stress, p is the pressure, and A is the area parallel to the flow.

The Reynolds number Re , defined by

$$Re = \frac{Uh}{\nu} \quad (5),$$

was computed at the OD for all arms (listed in Table 8), using the disk surface speed at the disk edge, $U @ 44 \text{ m/s}$, the kinematic viscosity of air, $\nu = 1.512 \times 10^{-5} \text{ m}^2/\text{s}$, and the appropriate distance between the arm surface and the disk, h . Since Re was lower than 2000 for all arms, the flow between the arm and the disk can be assumed to be a Couette flow and the shear stress $\hat{\tau}$ is expressed by

$$\hat{\tau} = \mu \frac{U}{h} \quad (6),$$

where μ is the fluid static viscosity. Increasing the arm thickness results in a smaller spacing h between the arm surface and the disk and an increased area A parallel to the

flow, which leads to a higher shear stress according to Eq. (6), and that in turn leads to a higher friction drag force D_f according to Eq. (3). Increasing the arm thickness also results in an increased area S normal to the flow, which leads to a higher pressure drag force D_p , according to Eq. (4). Consequently, increasing the E-block arm thickness yields a higher drag force, and that may have generated higher levels of vibration.

The 2-20 kHz RMS component amplitudes were further broken down into three subcomponents in the 2-6 kHz, 6-10 kHz, and 10-20 kHz frequency bands in order to assess the contributions resulting primarily from suspension dynamics (2-6 kHz and 10-20 kHz bands), and those resulting primarily from E-block arm dynamics (6-10 kHz band). These RMS component amplitudes are listed in Tables 9 through 11 and are plotted in Figs. 16 through 18.

An examination of the component plots in Figs. 16 through 18 indicates that the component amplitudes increased as the slider was moved from the ID to the OD, and that this trend was most pronounced for the suspension second torsion and sway modes, which are captured in the 10-20 kHz frequency band.

The first torsion mode of the HGA occurs at around 4 kHz, but there is no peak at this frequency in any of the power spectra, which indicates that this mode was not excited to a significant level. This explains the lack of dependency of the RMS amplitude components in the 2-6 kHz frequency band on arm thickness, as evident from Fig. 16.

Figure 17 indicates that the RMS amplitude components in the 6-10 kHz frequency band are dependent on arm thickness. The main mode excited in this frequency band is the sway mode of the E-block arm, which occurs at around 8 kHz. Going from the 1.0 mm thick arm to the 1.6 mm thick arm, the RMS amplitude components in Fig. 17 attained their highest values at the 1.2 mm thickness and then decreased to attain their lowest values at the 1.6 mm thickness for all radial positions. This is the same trend that was observed in the 2-20 kHz component amplitudes.

The variation of the RMS component amplitudes in the 10-20 kHz band (Fig. 18) as a function of E-block arm thickness followed a similar trend to that observed for the RMS component amplitudes in the 6-10 kHz band, although the effect was on a much smaller scale. This trend is likely to be a result of the dynamic coupling between the E-block arm and the suspensions.

The variation of the RMS amplitude of the slider off-track vibration over the 2-20 kHz frequency range as a function of E-block arm thickness was primarily shaped by the 6-10 kHz component, as evident from Figs. 15 and 17.

5. Conclusion

In this study, the effect of E-block arm thickness on the off-track vibration of a read/write head inserted between two co-rotating disks was investigated experimentally in a modeled hard disk drive. Four different E-block arm thicknesses were used, ranging from 1.0 mm to 1.6 mm in steps of 0.2 mm. Head vibration in the off-track direction was measured at the ID, the MD, and the OD positions. For each E-block arm thickness, the head exhibited the highest level of off-track vibration at the outer diameter, and the lowest level of off-track vibration at the inner diameter.

The primary contributors to the measured off-track vibration were identified as the E-block arm sway mode, the suspension second torsion mode, and the suspension sway mode. The off-track RMS amplitudes were broken down into components over two frequency bands (0-2 kHz and 2-20 kHz) in order to assess the contribution of the structural resonances to the overall head off-track vibration. The 2-20 kHz component was further divided into subcomponents over three frequency bands in order to isolate the contributions of the E-block arm vibration and the suspension vibration to off-track RMS amplitudes.

The measured off-track RMS amplitudes were dependent on the E-block arm thickness. The RMS amplitudes, for all radial positions, increased as the arm thickness was increased. This trend was also observed in the 0-2 kHz component amplitudes. This trend, however, was not observed in the 2-20 kHz component amplitudes. The latter

amplitudes increased as the arm thickness was increased to attain their highest values at the 1.2 mm arm thickness, and then decreased as the arm thickness was increased further to attain their lowest values at the 1.6 mm thickness. This trend in the observed off-track vibration was strongly shaped by the component of off-track resulting from the E-block arm dynamics.

An investigation of the effect of arm thickness on the airflow in the modeled drive will be extremely helpful in explaining the results presented in this study, especially the unexpected trend observed in the 2-20 kHz component.

6. Acknowledgements

This study was supported by the Computer Mechanics Laboratory at the University of California at Berkeley, the Hard Disk Drive Division at Fujitsu Ltd., and the Information Storage Industry Consortium.

7. References

- [1] Yamaguchi, Y., Takahashi, K., Fujita, H. and Kuwahara, K., "Flow Induced Vibration of Magnetic Head Suspension in Hard Disk Drive", IEEE Transaction on Magnetics, Vol. 22, No. 5, September 1986, pp. 1022-1024.

- [2] Yamaguchi, Y., Talukder, A.A., Shibuya, T. and Tokuyama, M., "Air Flow Around a Magnetic-Head-Slider Suspension and Its Effect on Slider Flying-Height Fluctuation", IEEE Transaction of Magnetics, Vol. 26, No. 5, September 1990, pp. 2430-2432.

- [3] Tokuyama, M., Yamaguchi, Y., Miyata, S. and Kato, C., "Numerical Analysis of Flying-Height Fluctuation and Positioning Error of Magnetic Head due to Flow Induced by Disk Rotation", IEEE Transaction of Magnetics, Vol. 27, No. 6, November 1991, pp. 5139-5141.

- [4] Iglesias, I. and Humphrey, J., "Two- and Three-Dimensional Laminar Flows Between Disks Co-Rotating in a Fixed Cylindrical Enclosure", International Journal for Numerical Methods in Fluids, Vol. 26, 1998, pp. 581-603.

- [5] Abrahamson, S., Chiang, C. and Eaton, J.K., "Flow Structure in Head-Disk Assemblies and Implications for Design", Advanced Information Storage Systems, Vol. 1, 1991, pp. 111-132.

- [6] Harrison, J.C., Lou, D.H. and Talke, F.E., "AirFlow at the Tip of an Obstruction Between Corotating Disks", *Advanced Information Storage Systems*, Vol. 5, 1993, pp. 159-174.
- [7] Suzuki, H. and Humphrey, J., "Flow Past Large Obstructions Between Corotating Disks in Fixed Cylindrical Enclosures", *ASME Journal of Fluids Engineering*, Vol. 119, September 1997, pp. 499-505.
- [8] Girard, J., Abrahamson, S. and Uznanski, K., "The Effect of Rotary Arms on Corotating Disk Flow", *ASME Journal of Fluids Engineering*, Vol. 117, June 1995, pp. 259-262.



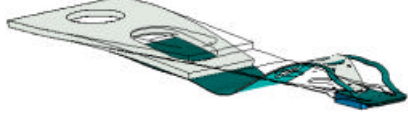
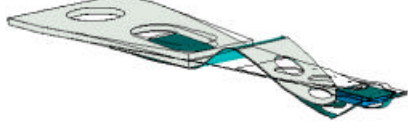
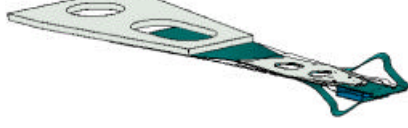



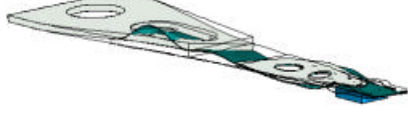

Natural Frequency [Hz]		Mode Shape
Upper	Lower	
2,200	2,200	Loadbeam first bending 
4,080	4,080	Loadbeam first torsion 
5,470	5,520	Baseplate first bending in phase with loadbeam second bending 
6,940	7,050	Baseplate first bending out of phase with loadbeam second bending 
12,960	12,960	Loadbeam second torsion 
13,100	13,080	Loadbeam third bending 
14,420	14,420	Loadbeam sway 
18,550	18,540	Loadbeam fourth bending 
19,070	17,350	Loadbeam third torsion in phase with baseplate first torsion 
20,130	19,790	Loadbeam third torsion out of phase with baseplate first torsion 

Table 1: HGA natural frequencies and mode shapes of active modes in 0-20 kHz range.


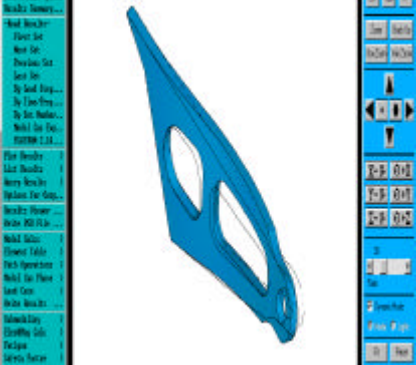


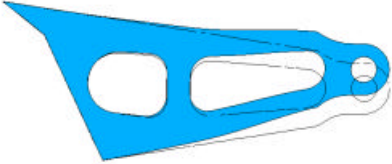
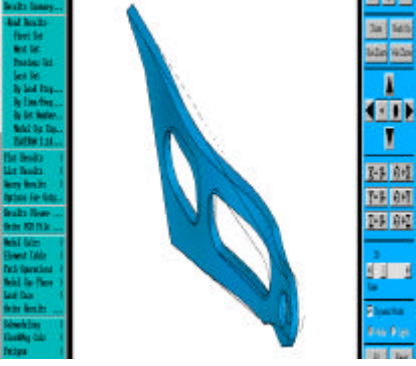

Natural Frequency [Hz]					Mode Shape
t = 1.0	t = 1.2	t = 1.4	t = 1.6		
2,000	2,500	3,000	3,500	First bending	
9,160	11,020	12,810	14,520	Second bending	 
11,230	13,340	15,400	17,420	First torsion	
13,860	14,290	14,610	14,870	Sway	
22,970	27,240	31,270	35,030	Third bending	 

Table 2: E-block arm natural frequencies and mode shapes of first five modes.

Mode Shape	Natural Frequencies [Hz]			
	t =1.0	t =1.2	t =1.4	t =1.6
E-block sway coupled with suspension sway	9,200	9,720	10,150	1,0500
E-block first torsion coupled with suspension third bending	9,120	10,450	11,510	13,420
Suspension second torsion (upper and lower suspensions in phase)	12,960	12,970	12,940	12,920
Suspension second torsion (upper and lower suspensions out of phase)	12,960	13,010	13,040	13,070
Suspension sway (upper and lower suspensions in phase)	14,030	14,180	14,300	14,350
Suspension sway (upper and lower suspensions out of phase)	14,460	14,490	14,600	14,400

Table 3: FEA results for the natural frequencies and mode shapes of the HSA modes that were identified in the experimental measurements.

Mode Shape	Resonance Frequencies [Hz]			
	t =1.0	t =1.2	t =1.4	t =1.6
E-block sway coupled with suspension sway	7,450	7,950	8,130	8,330
E-block third torsion coupled with suspension second bending	9,120	10,450	11,510	13,420
Suspension second torsion	12,700	12,200	12,230	12,530
Suspension sway	13,750	14,100	14,130	14,050

Table 4: Estimates of the frequencies of the three dominant resonant peaks observed in the measured spectra.

Thickness [mm]	ID	MD	OD
1.0	4.15	5.95	7.67
1.2	5.21	6.82	7.73
1.4	5.29	7.48	10.12
1.6	5.42	9.34	10.51

Table 5: RMS amplitudes [nm] of the slider off-track vibration over the 0-20 kHz frequency range.

Thickness [mm]	ID	MD	OD
1.0	2.43	2.92	3.63
1.2	3.28	3.70	5.30
1.4	3.79	5.39	7.32
1.6	4.53	8.24	9.00

Table 6: RMS amplitudes [nm] of the slider off-track vibration over the 0-2 kHz frequency range.

Thickness [mm]	ID	MD	OD
1.0	3.37	5.20	6.77
1.2	4.06	5.74	7.86
1.4	3.69	5.20	7.02
1.6	2.99	4.40	5.44

Table 7: RMS amplitude components [nm] of the slider off-track vibration over the 2-20 kHz frequency range.

Thickness [mm]	h [mm]	Re
1.0	0.5	1460
1.2	0.4	1160
1.4	0.3	870
1.6	0.2	580

Table 8: Reynolds number at OD for different arm thicknesses.

Thickness [mm]	ID	MD	OD
1.0	1.22	1.46	1.63
1.2	0.84	1.09	1.28
1.4	0.95	1.16	1.49
1.6	0.86	1.07	1.25

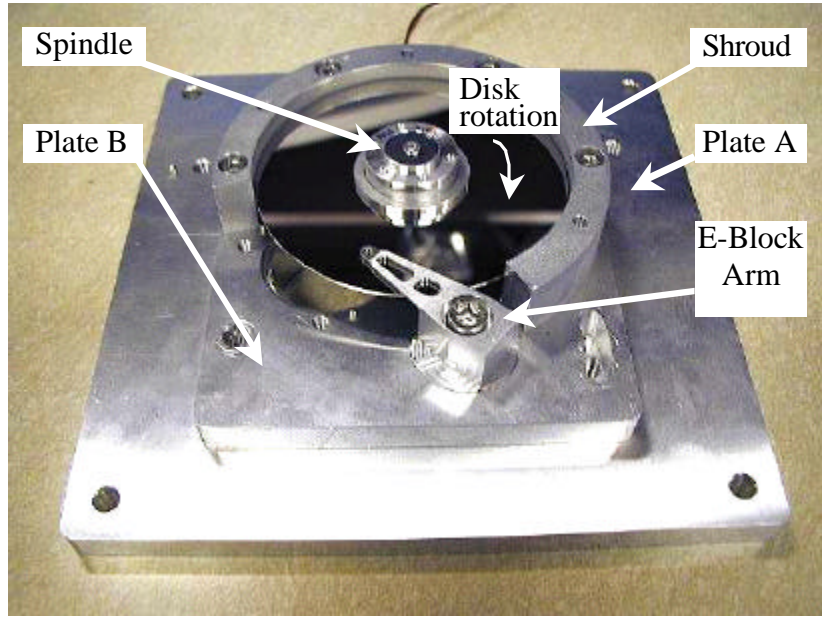
Table 9: RMS amplitude components [nm] of the slider off-track vibration over the 2-6 kHz frequency range.

Thickness [mm]	ID	MD	OD
1.0	2.40	2.35	2.94
1.2	2.99	3.66	4.74
1.4	2.43	2.63	3.33
1.6	1.72	1.72	2.38

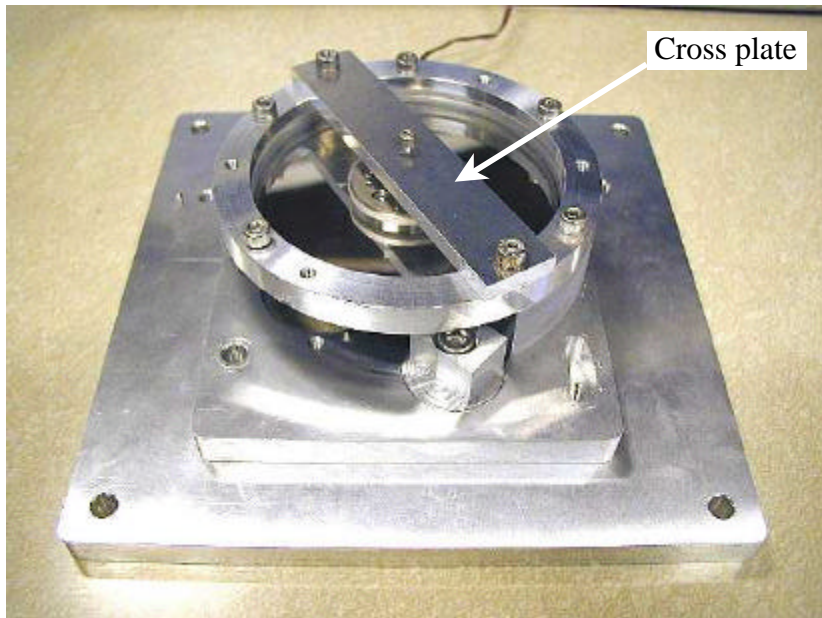
Table 10: RMS amplitude components [nm] of the slider off-track vibration over the 6-10 kHz frequency range.

Thickness [mm]	ID	MD	OD
1.0	2.01	4.39	5.88
1.2	2.61	4.28	6.14
1.4	2.61	4.33	5.99
1.6	2.29	3.90	4.73

Table 11: RMS amplitude components [nm] of the slider off-track vibration over the 10-20 kHz frequency range.



(a) Setup without top disk and cover



(b) Setup with top disk and cover

Figure 1: Modeled disk drive.

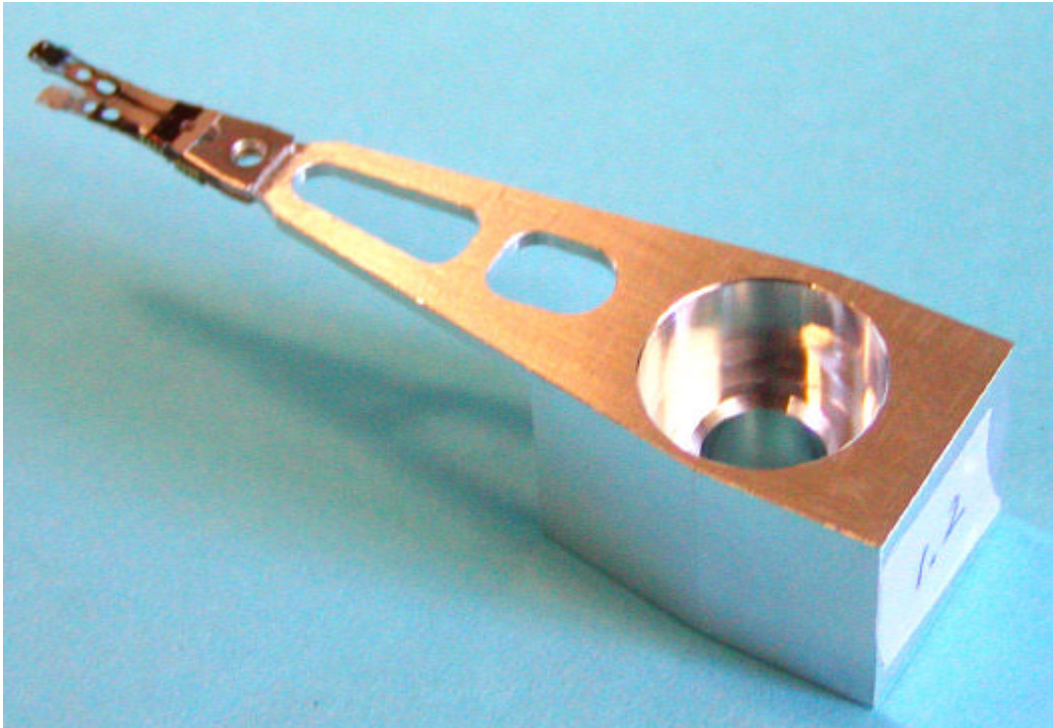


Figure 2: A close-up of the HSA.

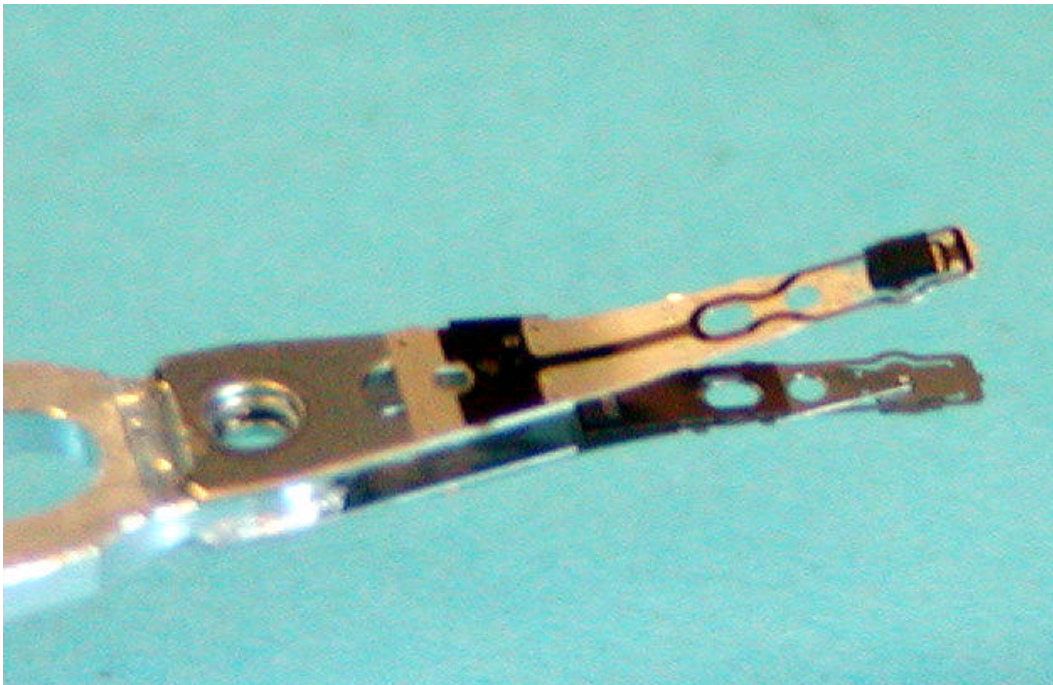


Figure 3: A close-up of the HSA.

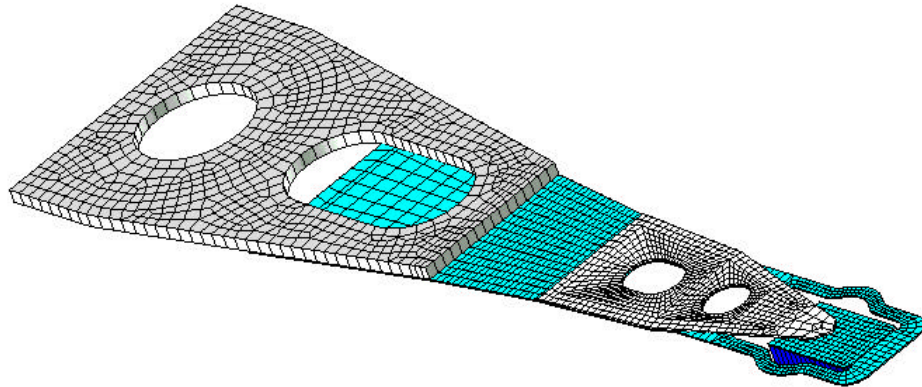


Figure 4: ANSYS model of pico-CAPS HGA.

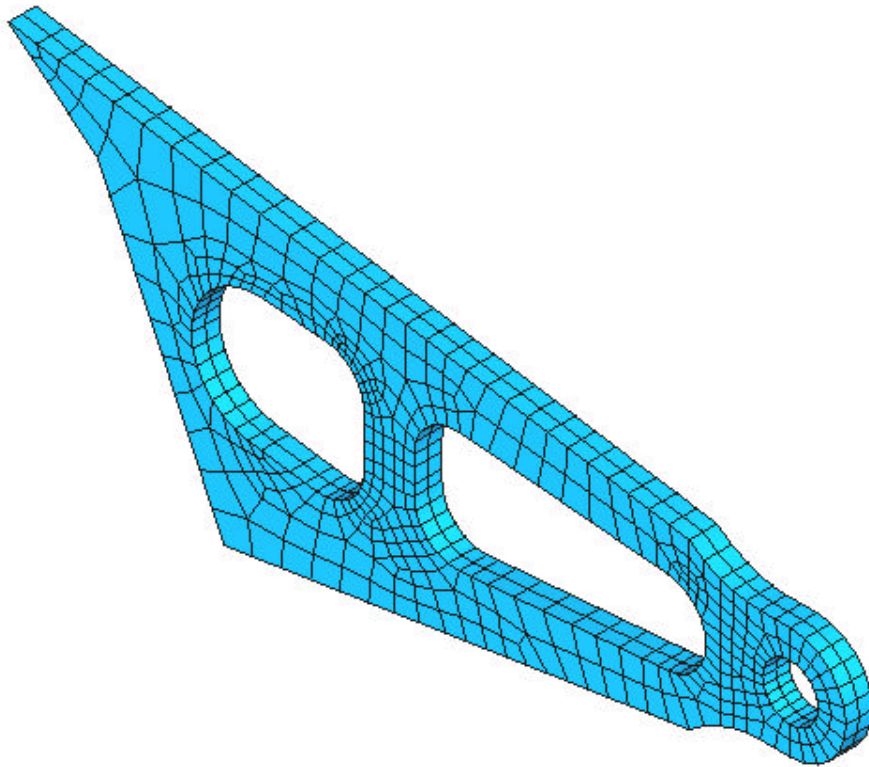


Figure 5: ANSYS model of E-block arm.

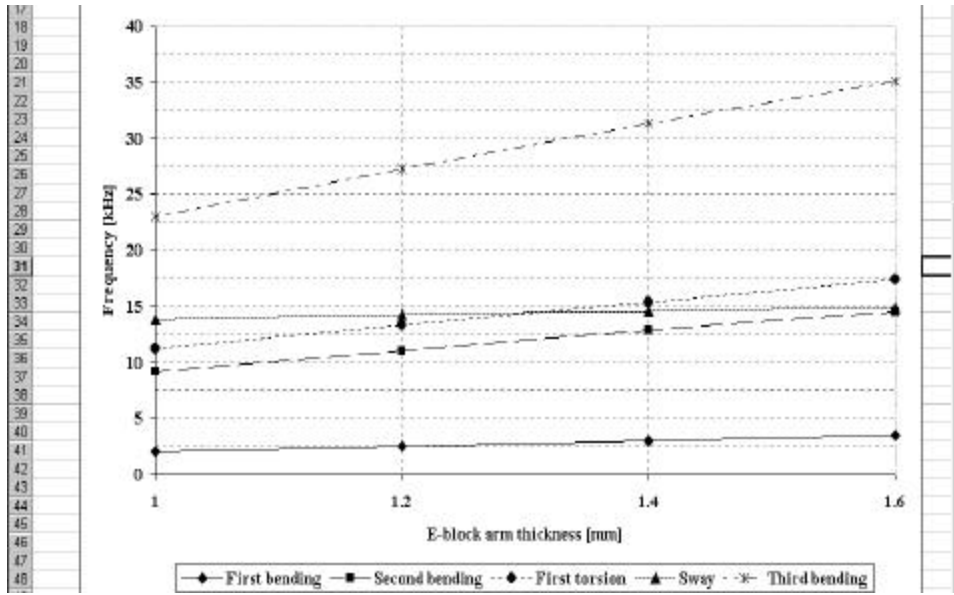


Figure 6: Variation of the natural frequencies of the first five E-block modes as a function of E-block arm thickness.

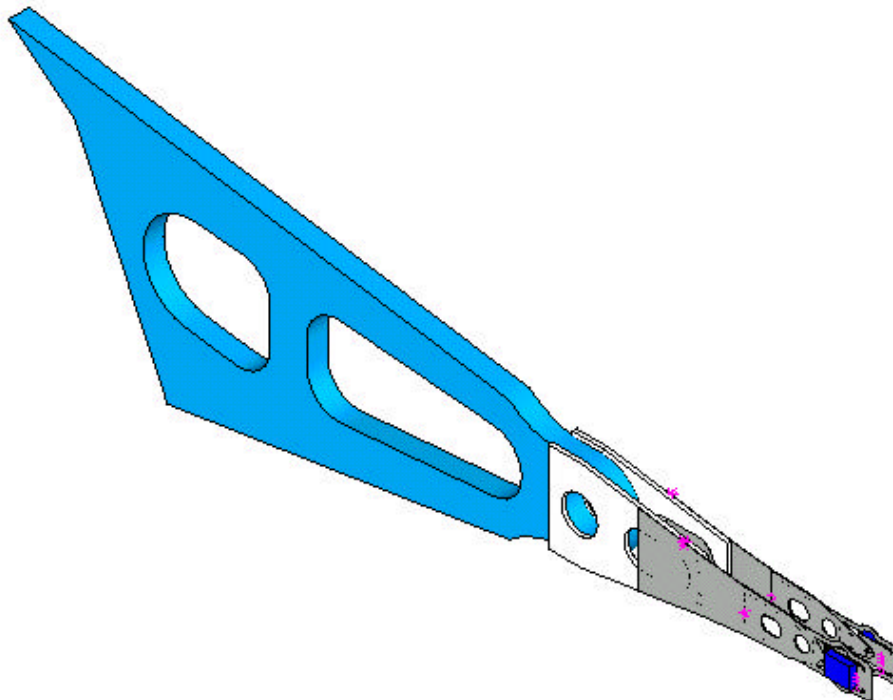


Figure 7: ANSYS HSA model.

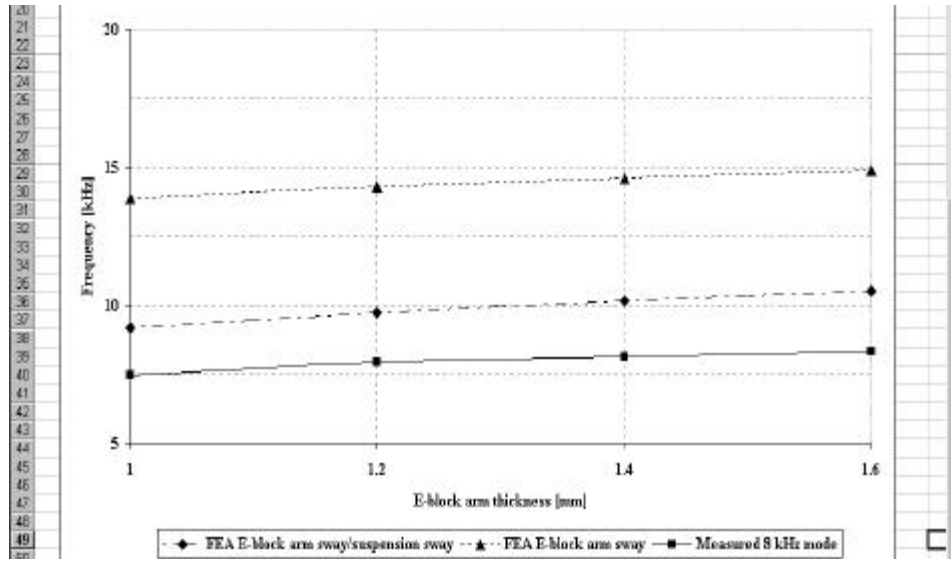
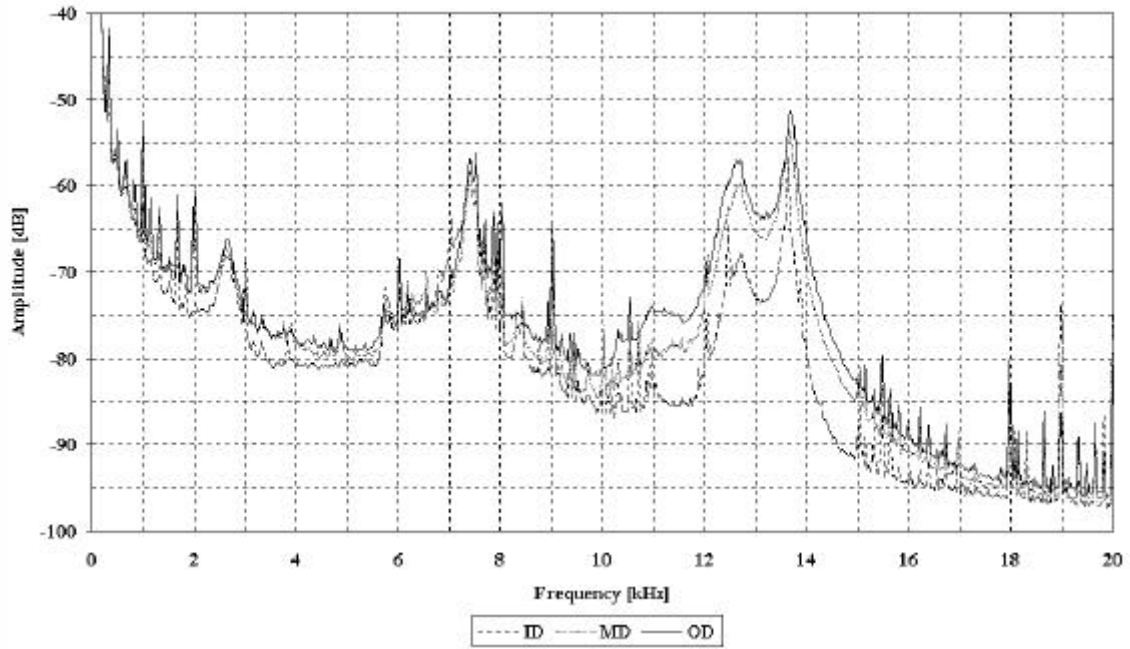
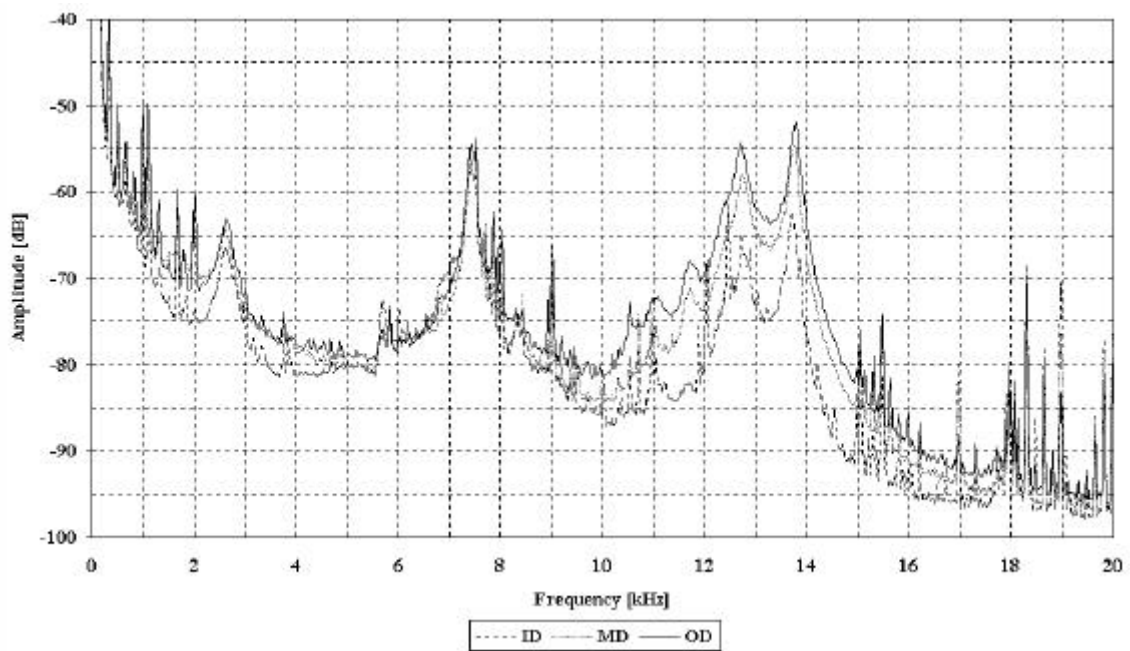


Figure 8: Variation of resonant frequencies of different thickness arms.

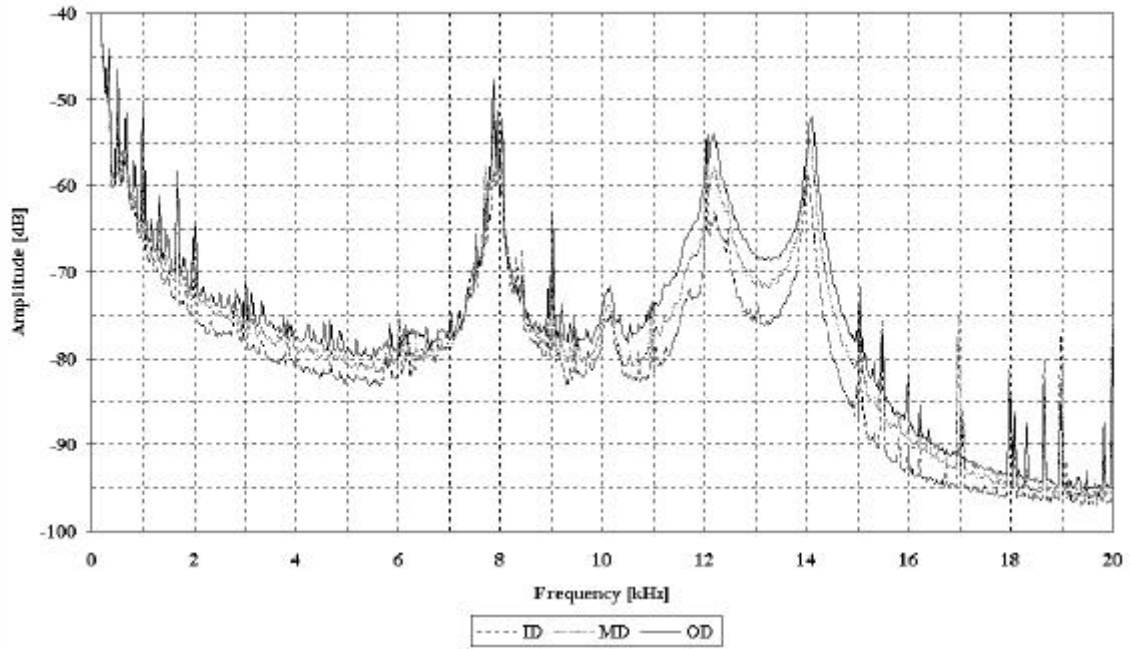


(a) Sample 1

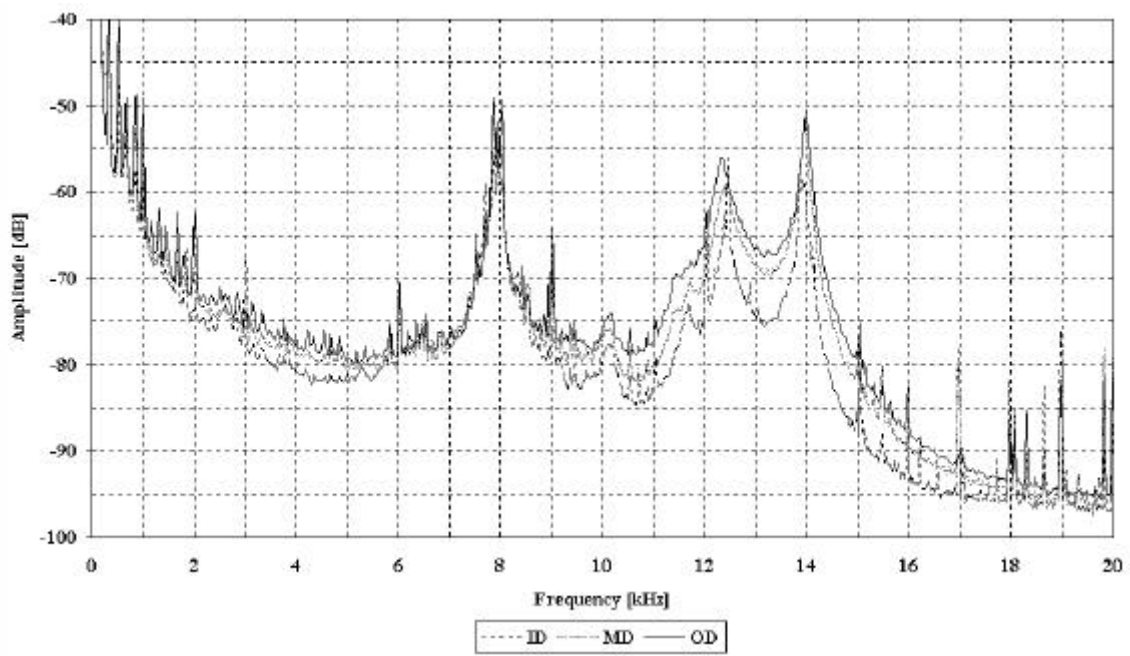


(b) Sample 2

Figure 9: Power spectrum of slider off-track vibration, 1.0 mm thickness arm
 (a) Sample 1; (b) Sample 2

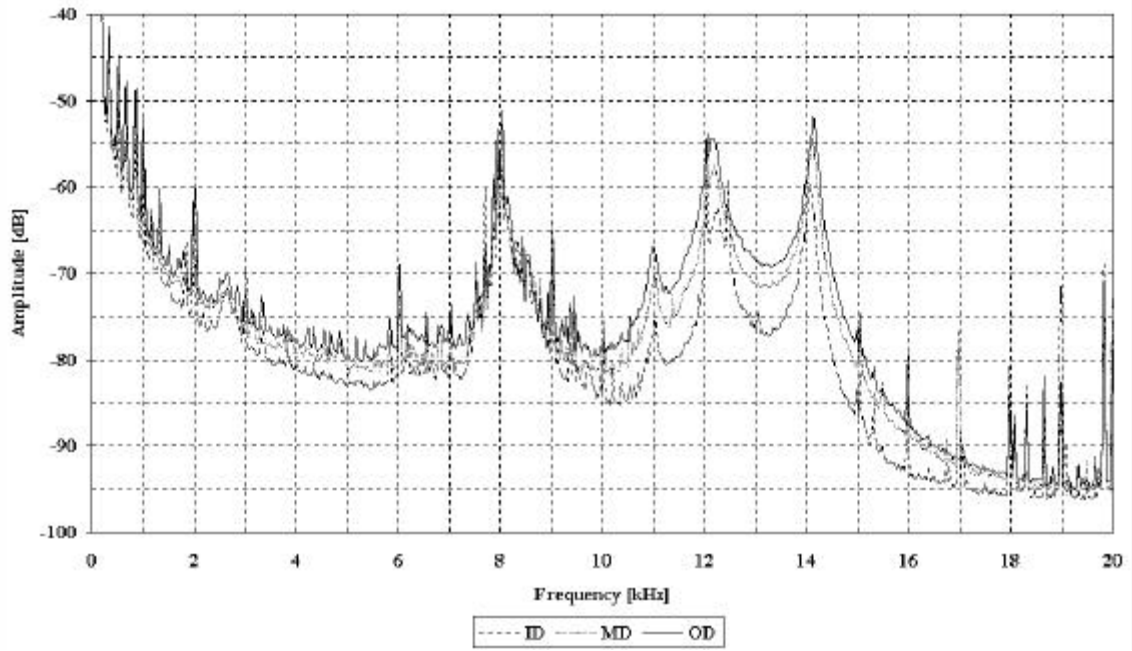


(a) Sample 1

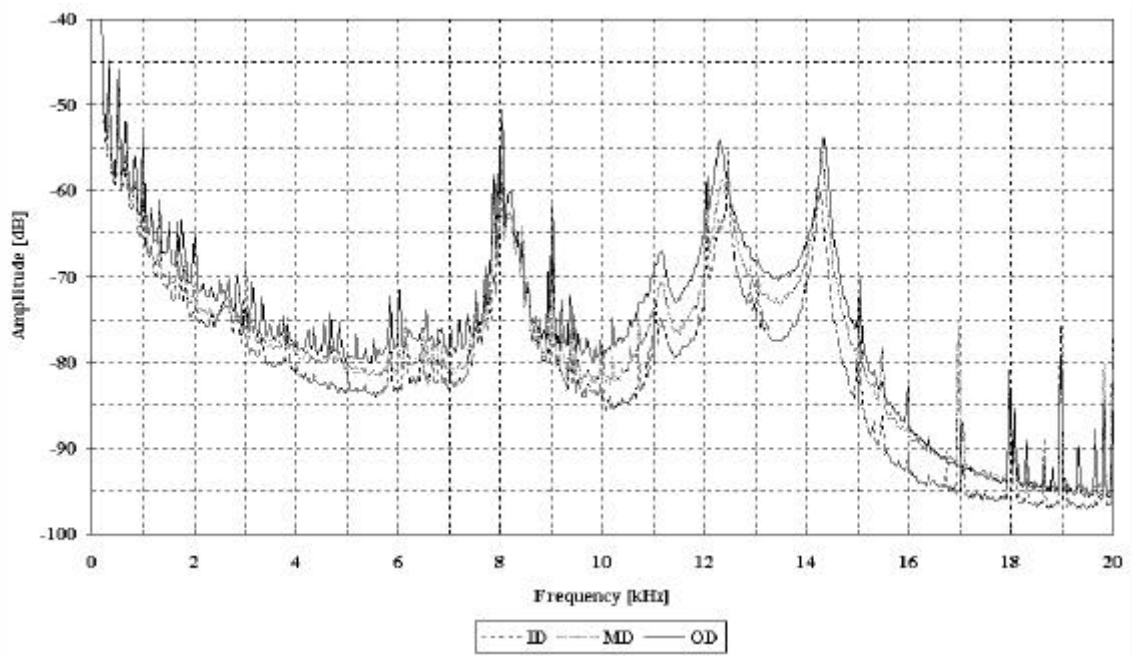


(b) Sample 2

Figure 10: Power spectrum of slider off-track vibration, 1.2 mm thickness arm
 (a) Sample 1; (b) Sample 2

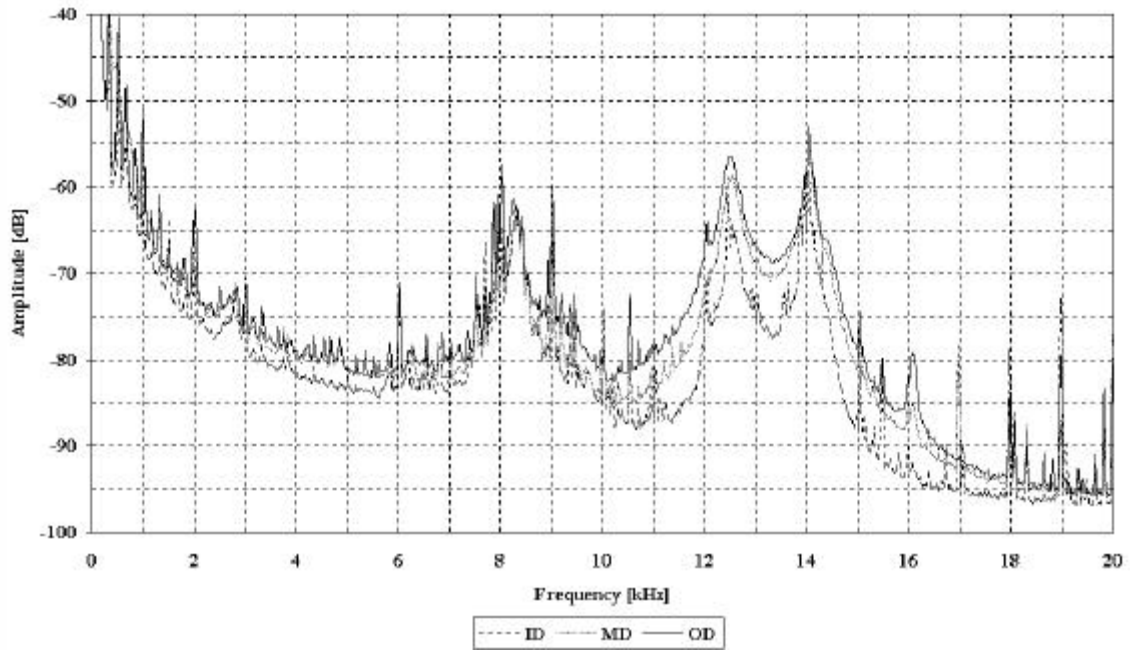


(a) Sample 1

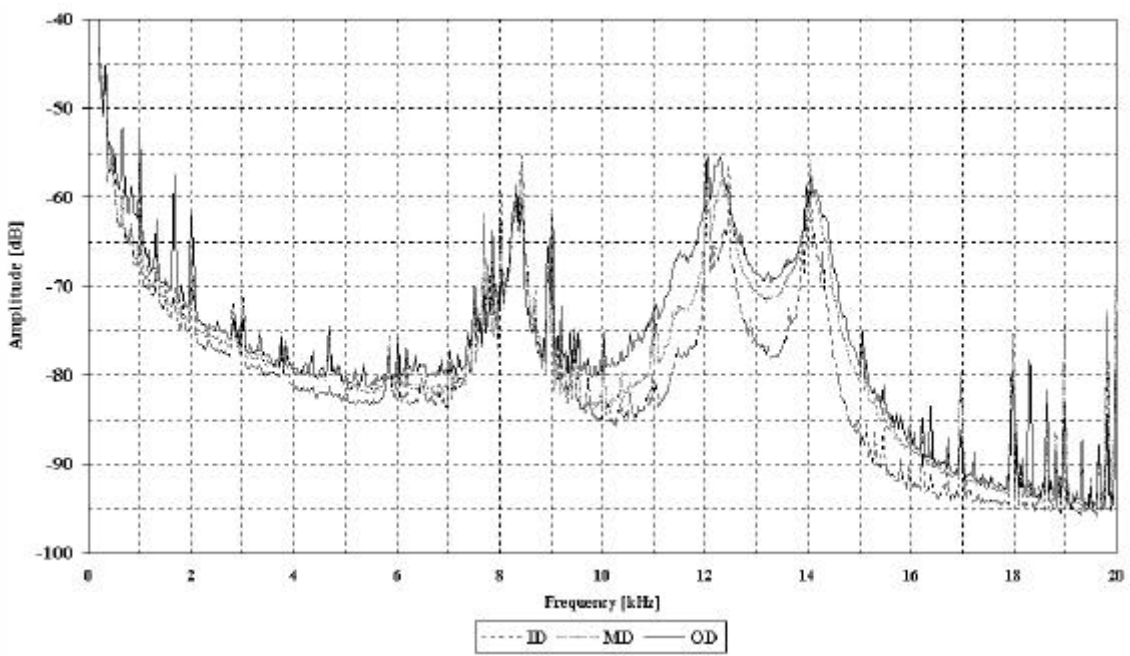


(b) Sample 2

Figure 11: Power spectrum of slider off-track vibration, 1.4 mm thickness arm.
 (a) Sample 1; (b) Sample 2



(a) Sample 1



(b) Sample 2

Figure 12: Power spectrum of slider off-track vibration, 1.6 mm thickness arm
 (a) Sample 1; (b) Sample 2

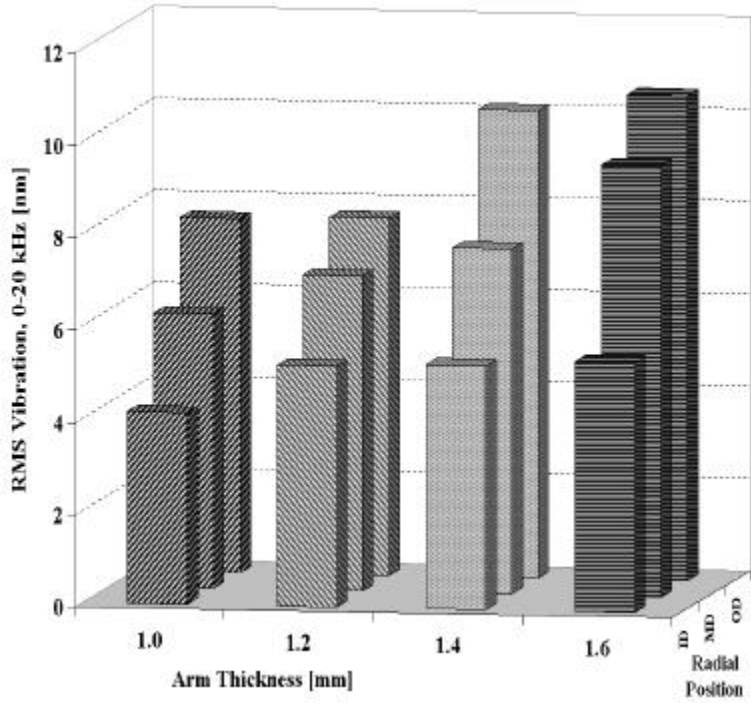


Figure 13: RMS amplitudes [nm] of the slider off-track vibration over the 0-20 kHz frequency range.

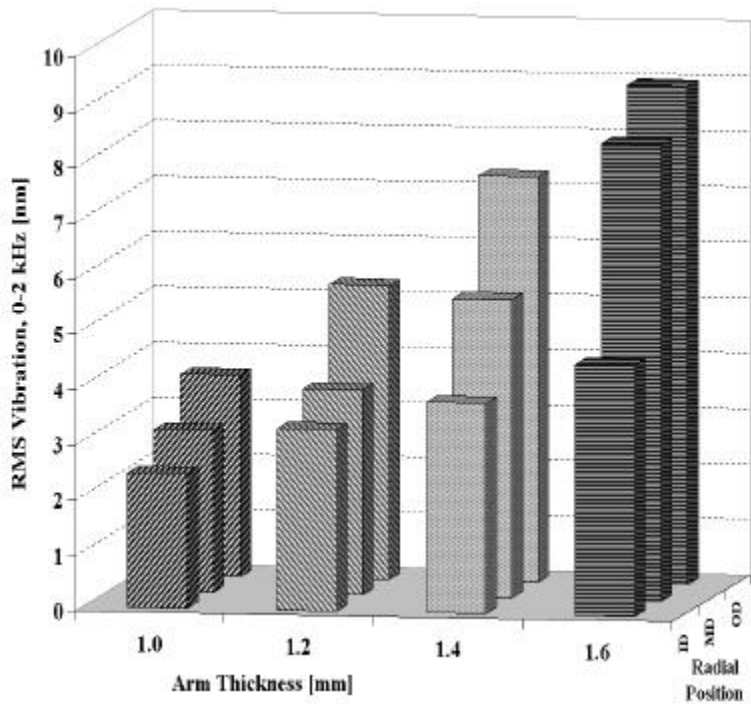


Figure 14: RMS amplitude components [nm] of the slider off-track vibration over the 0-2 kHz frequency range.

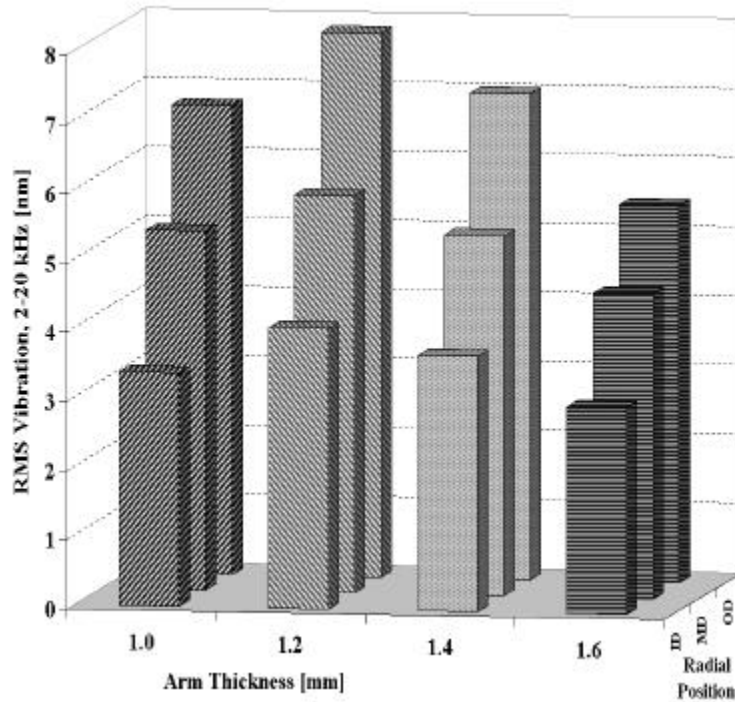


Figure 15: RMS amplitude components [nm] of the slider off-track vibration over the 2-20 kHz frequency range.

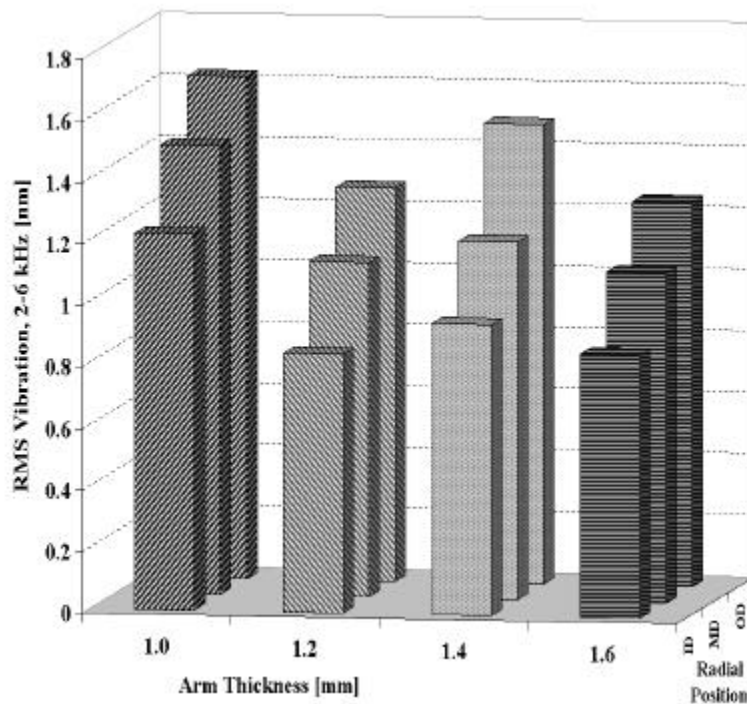


Figure 16: RMS amplitude component [nm] of the slider off-track vibration over the 2-6 kHz frequency range.

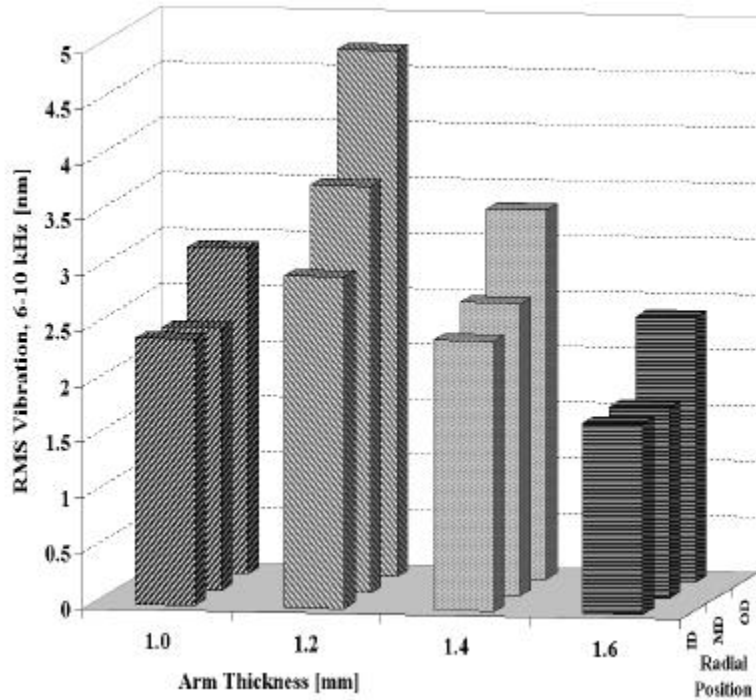


Figure 17: RMS amplitude component [nm] of the slider off-track vibration over the 6-10 kHz frequency range.

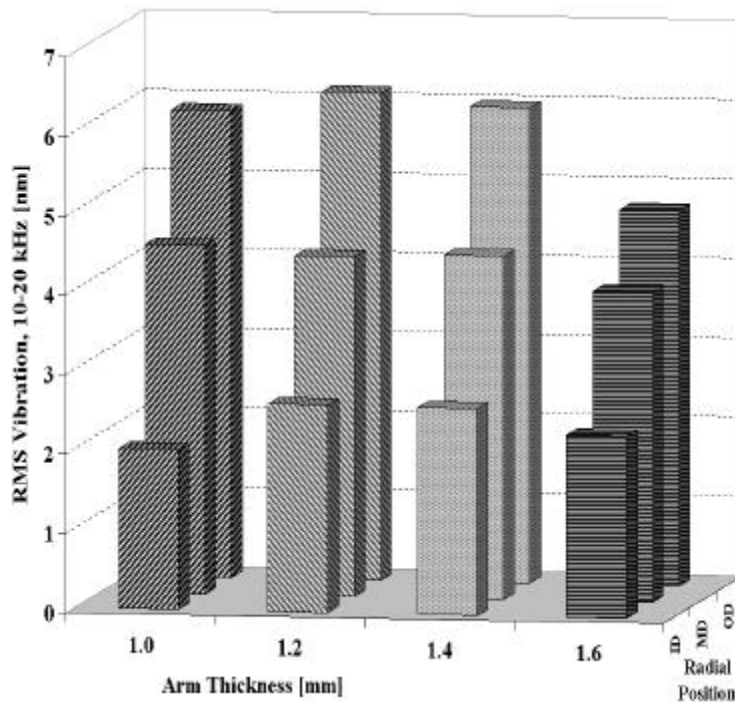


Figure 18: RMS amplitude component [nm] of the slider off-track vibration over the 10-20 kHz frequency range.